Strontium Doped Hydroxyapatite Nanoparticles: Synthesis, Characterization and Simulation

ZHOU Zihang[1], WANG Qun[2], GE Xiang[3], LI Zhaoyang[1]

(1. School of Materials Science and Engineering, Tianjin University, Tianjin 300350, China; 2. College of Life Science and Biotechnology, MianYang Teachers' College, Mianyang 621006, China; 3. Key Laboratory of Mechanism Theory and Equipment Design of Ministry of Education, School of Mechanical Engineering, Tianjin University, Tianjin 300354, China)

Abstract: Strontium (Sr) doped hydroxyapatite (HA) has been widely used in diverse biological applications. In this work, hydrothermal synthesis method was used to prepare HA and Sr doped HA nanoparticles. A series of experimental methods and the simulation method based on density functional theory (DFT) were used to investigate the effect of Sr doping on chemical composition, crystallinity, lattice parameters, morphology, and formation energies of HA. The experimental results indicated that the lattice parameters and crystal size of Sr doped HA nanoparticles increased. The crystallinity of Sr doped HA nanoparticles did not change significantly with the increasing concentration of Sr ions. The lattice parameters obtained by the simulation method were in good agreement with the experimental results. The formation energies indicated that Sr ion doping endowed the structure more stable, which also illustrated that the Ca(1) site was the preferential site for Sr doping at 10at% and mixed doping was a more preferred doping mode at 50at%.

Key words: hydroxyapatite; strontium doping; lattice parameter; density functional theory; formation energy

Hydroxyapatite (HA) has been widely used as a bio-ceramic with good biological activity. HA plays an important role in dental and bone regeneration due to its superior biocompatibility and excellent ability to bond bone tissue [1]. However, the crystallinity, morphology, and other physical properties are different between biological apatites and pure HA[2]. In order to modify the solubility and degradation of HA, as well as to add some additional biological and antibacterial properties, many techniques have been employed[3-4]. Recently, introducing extrinsic ions, such as $Zn^{2+[5]}$, $Ba^{2+[6]}$, $F^{-[7-10]}$, into an apatite structure is the most practicable and effective method to solve these problems.

Sr is proved to be one of the most constituent elements in bones. It has been extensively utilized to endow HA with better performances, such as higher biocompatibility and bioactivity, due to its excellent biocompatibility[11-12]. *In vivo* and *in vitro* studies have demonstrated that Sr doping can significantly accelerate differentiation of osteoblast cells and inhibit proliferation of osteoclast cells[13-14]. The stoichiometric component of HA is $Ca_{10}(PO_4)_6(OH)_2$ and the unit cell of it belongs to $P6_3/m$ space group which has a C3 symmetry[15]. The Sr ions HA hexagonal structure can be doped into two types of Ca sites [Ca(1) and Ca(2)][16]. Four of the ten Ca sites, named as Ca(1), form channels parallel to the *c*-axis. Remaining six of the ten Ca sites, denoted as Ca(2), are located as two symmetrical triangles around hydroxyl channels[17-18]. Previous studies found that Sr ions could enter these two types of Ca sites without solubility limitation[19]. It is worth noting that Sr ions shows different site preference during the process of doping. Terra *et al.*[20] studied the site preference of Sr doping by Rietveld refinement of X-ray diffraction patterns when the doping molar concentrations of Sr are below 1%. Their results showed that the Ca(1) sites are the preferential site for Sr doping. Zeglinski *et al.*[17] utilized the density functional theory (DFT) method to study the most preferential mode and revealed that the mixed substitution occurred at Ca(1) and Ca(2) sites randomly and Ca(2) sites become the

preferential sites with the increase of substitution concentration of Sr ions. Bigi et al.[19] reported a preference for the Ca(2) substitution at or above 10at% of Sr, while Ca(1) was preferred at 5at% of Sr. So far, there is still a controversy regarding the preferred doping sites of Sr ions in the HA crystal structure.

Although there have been many theoretical and experimental studies on Sr doping into HA structure, few studies have combined theory with experimental results. In this study, a hydrothermal method was used to synthesize the pure HA and Sr doped (10at%, 50at%, 100at%) HA nanoparticles. Scanning electron microscopy (SEM), X-ray diffraction (XRD), high-resolution transmission electron microscopy (HRTEM), and selected-area electron diffraction (SAED) were employed to provide the morphology, crystallinity, and microstructure of the samples. *Ab initio* method which is based on quantum mechanics provided the lattice parameters and formation energy according to Sr doping concentrations. The preference sites of Sr ions doping for Ca at 10at% and 50at% concentration were also discussed.

1 Materials and methods

1.1 Preparation of HA and Sr-HA

HA ($Ca_{10}(PO_4)_6(OH)_2$) and Sr-doped HA ($Ca_{10-x}Sr_x(PO_4)_6(OH)_2$, $x=0-10$) nanoparticles with Sr concentrations at 10at%, 50at%, 100at% ($x=1, 5, 10$) were prepared by a hydrothermal method. Calcium nitrate tetrahydrate ($Ca(NO_3)_2 \cdot 4H_2O$), strontium nitrate ($Sr(NO_3)_2$), and diammonium hydrogen phosphate ($(NH_4)_2HPO_4$) were utilized as Ca, Sr, and P sources, respectively. Preparation procedure of 2 g of 50at% Sr-doped HA was as follows: 1.9 g of $Ca(NO_3)_2 \cdot 4H_2O$, 1.703 g of $Sr(NO_3)_2$, and 1.275 g of $(NH_4)_2HPO_4$ were dissolved into 60 mL deionized water. Then, 25% ammonia solution was used to adjust the pH between 10 and 10.5. After stirring the mixture for 5 min, it was injected into a hydrothermal reactor and aged at 150 ℃ for 6 h. The precipitates obtained by centrifugation were cleaned three times with distilled water and anhydrous ethanol. Finally, the products were dried at 70 ℃ for 12 h.

1.2 Characterization of the samples

Lattice parameters (*a* and *c*) were quantified from peaks of (002) and (211) in an XRD pattern, respectively, using the standard hexagonal close packed unit cell plane spacing relationship[21]:

$$\frac{1}{d^2} = \frac{4}{3}\left(\frac{h^2+k^2+l^2}{a^2}\right) + \frac{c^2}{l^2} \qquad (1)$$

where *d* is the distance between two adjacent planes in the set of Miller indices (*hkl*).

The degree of crystallinity[22], corresponding to the fraction of crystalline phase present in the examined volume, was evaluated as:

$$X_c = 1 - \left(\frac{V_{112/300}}{I_{300}}\right) \qquad (2)$$

where I_{300} is the intensity of (300) reflection and $V_{112/300}$ is the intensity of the hollow between (112) and (300) reflections, which completely disappears in non-crystalline samples.

Composition of individual apatite crystals was examined by X-ray energy dispersive spectrometer (EDS) equipped on SEM. The atomic concentrations of elements (Ca, P, and Sr) in the nanoparticles were further determined by an inductive coupled plasma emission spectrometer (ICP; VISTA-MAX) method.

Surface morphology of the synthesized HA nanoparticles were observed by SEM (HITACHI S-4800, Tokyo, Japan) at an accelerating voltage of 5 kV. The phase analysis was carried out using X-ray powder diffraction instrument (RIGAKU/DMAX). The patterns were recorded using CuKα radiation in the 2θ range of 10–90° at the step size of 0.02° with the scan speed of 8 (°)/min.

The microstructures of nanoparticles were examined by TEM for comparing with XRD results. TEM images were taken using a JEM-2100F microscope at 200 kV. HRTEM images and SAED patterns were also obtained.

1.3 Computational method

The calculations were carried out using the CASTEP module in the Materials Studio software package. The CASTEP code is an *ab initio* program which can calculate ground state energies of atomic systems accurately based on DFT. The two types of Ca sites [Ca(1) or Ca(2)], with four Ca(1) sites surrounded by nine oxygen atoms and six Ca(2) sites positioning around the OH groups, can be substituted by other doping cations. Based on the unit cell of HA, eight possible Sr-doped HA models were built.

1Sr-Ca(1)-HA model: One Ca(1) was replaced by one Sr atom in pure HA.

4Sr-Ca(1)-1Sr-Ca(2)-HA model: Four Ca(1) were replaced by four Sr atoms and one Ca(2) was replaced by one Sr atom in pure HA.

Similarly, 1Sr-Ca(2)-HA, 3Sr-Ca(1)-2Sr-Ca(2)-HA, 2Sr-Ca(1)-3Sr-Ca(2)-HA, 1Sr-Ca(1)-4Sr-Ca(2)-HA, 5Sr-Ca(2)-HA and 10Sr-HA models were built. The stable models after geometric optimization (pure HA, 1Sr-Ca(1)-HA, 2Sr-Ca(1)-3Sr-Ca(2)-HA and 10Sr-HA) are optimized.

All calculations of structure optimization were conducted by the generalized gradient approximation (GGA) of the Perdew-Burke-Ernzerhof (PBE) exchange-correlation which was based on an energy minimization principle.

The electronic ground state was achieved using a conjugate. The Broyden-Fletcher-Goldfarb-Shanno (BFGS) was utilized to relax the atomic structure. The cutoff energy of the plane waves which was set as 380 eV and the Brillouin zone samplings with a k-point grid of 4×4×4 samplings were sufficient to guarantee the convergence of total energy. The convergence criteria of geometric optimization and energy were set to (a) a self-consistent field tolerance of 10^{-6} eV/atom, (b) an energy tolerance of 10^{-5} eV/atom, (c) a maximum force tolerance of 0.3 eV/nm, (d) a maximum stress tolerance of 0.05 GPa, and (e) a maximum displacement tolerance of 10^{-4} nm. The cell sizes and atomic positions were fully relaxed without any constraints in the process of DFT calculation.

To determine the most stable Sr-doped HA models, the formation energies of different substitution models were calculated by DFT method. The formation energy was evaluated by the following equation[23]:

$$E_{form}=E_{doped-HA}-(E_{HA}-n_i\mu_{Ca}+n_i\mu_{Sr}) \quad (3)$$

where E_{HA} is the energy of perfect HA and $E_{doped-HA}$ is the energy of doped-HA. n_i denotes the numbers of the corresponding ionic species to be removed from ($n_i>0$) or added ($n_i<0$) to the HA unit cell. The chemical potentials for Ca^{2+} and Sr^{2+} are given by μ_{Ca} and μ_{Sr}, respectively. In this study, the chemical potentials are approximated by their energies at 0 K.

2   Results and discussion

2.1   Chemical composition

Atomic concentrations of Ca, Sr, and P in the nanoparticles were examined by EDS, and the element content was further confirmed by ICP, as listed in Table 1 and Table 2. The results obtained by EDS and ICP were consistent. The ratios of various elements were nearly the same as the raw ratios before the hydrothermal synthesis. The molar ratios of Ca/P in HA and (Ca+Sr)/P in Sr-HA were around 1.67 which was close to the stoichiometric number of pure HA without any significant change after addition of Sr ions, which is similar to previous studies[18-19].

2.2   Analysis of XRD patterns

The XRD patterns of particles with different Sr doping concentrations from 0 to 100at% are shown in Fig. 1. The diffraction peaks of (002) and (300) shifted to a low 2θ value with gradual addition of Sr ions, illustrating an increase of lattice parameters (*a* and *c*) and *d*-spacings. This is because radius of Sr ion (0.118 nm) is larger than the radius of Ca ion (0.099 nm). These results were in line with those of previous studies[18, 24-26]. The characteristic diffraction peaks of all XRD patterns were narrow, suggesting good crystallinity of HA and all types of Sr-doped HA nanoparticles. The crystallinity and lattice parameters of all nanoparticles are shown in Table 3. Compared

Table 1   Chemical composition of nanoparticles measured by EDS

Sample	Ca/mol%	Sr/mol%	P/mol%	$n(Ca+Sr)/n(P)$	$n(Ca)/n(P)$	$n(Sr)/n(P)$	$n(Sr)/n(Ca+Sr)$
HA	62.02	0.03	37.95	–	1.634	–	–
10%Sr-HA	55.98	5.64	38.38	1.605	1.459	0.147	0.092
50%Sr-HA	31.85	30.59	37.56	1.662	0.847	0.814	0.490
100%Sr-HA	0.05	63.85	36.10	–	–	1.769	–

Table 2   Element content of nanoparticles measured by ICP

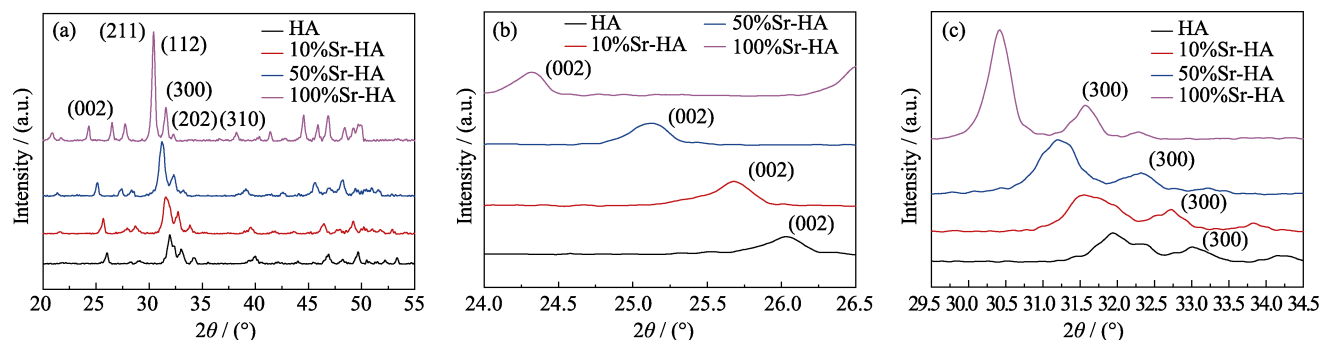| Sample	Ca/mol%	Sr/mol%	P/mol%	$n(Ca+Sr)/n(P)$	$n(Ca)/n(P)$	$n(Sr)/n(P)$	$n(Sr)/n(Ca+Sr)$
HA	62.19	0.06	37.75	–	1.647	–	–
10%Sr-HA	56.49	5.77	37.74	1.649	1.497	0.153	0.093
50%Sr-HA	31.85	30.57	37.58	1.660	10.848	0.813	0.490
100%Sr-HA	0.08	62.26	37.66	–	–	1.653	–

Fig. 1   (a) XRD patterns of HA and Sr-doped HA nanoparticles with (b) magnified (200) peaks, and (c) (300) peaks

Table 3 Lattice parameters and crystallinity of nanoparticles obtained by XRD

Sample	Crystallinity	$2\theta_{(002)}/(°)$	$2\theta_{(300)}/(°)$	a/nm	c/nm
HA	53.3%	26.07	33.09	0.93679	0.68286
10%Sr-HA	51.1%	25.68	32.76	0.94625	0.69326
50%Sr-HA	49.4%	25.12	32.34	0.95814	0.71056
100%Sr-HA	73.7%	24.34	31.58	0.98058	0.73071

with pure HA, crystallinites of 10%Sr-HA and 50%Sr-HA were slightly lower while 100%Sr-HA exhibited the highest crystallinity, in that doping of Sr ions can inhibit the growth of HA nanoparticles. When doping concentration of Sr ions is low, inhibition effect is more obvious, and the irregular grain size leads to crystallinity decrease. When the doping concentration is high up to 100%, it is more likely to form regular and large-size new grains, leading to crystallinity increase. The result was perfectly consistent with the previous report[23]. Wang *et al.*[23] reported that the crystallinities of Sr-doped HA nanoparticles decreased steadily with increasing Sr content in the range from 10mol% to 50mol%. When Sr reached 100mol%, the crystallinity increased suddenly[23].

2.3 Morphology by SEM observation

Fig. 2 clearly shows the morphologies of HA and Sr-doped HA nanoparticles. Agglomeration phenomenon occurred in all types of nanoparticles. The pure HA nanoparticles were rod-like. When the doped concentration of Sr increased from 10at% to 50at%, the morphology of Sr-doped HA did not change significantly compared with the pure HA. With the increase of Sr doping concentration, the crystal length increased, and the 100% Sr-HA nanoparticles presented rod-like shape and the largest crystal size. Geng *et al.*[18] also reported similar morphology changes.

2.4 Morphology and microstructure by TEM observation

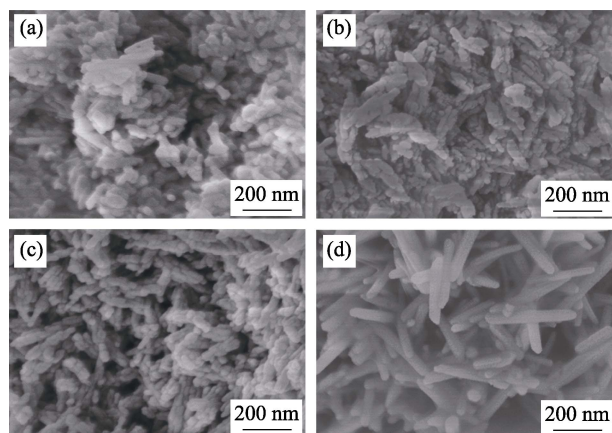TEM and SAED images of HA and all types of Sr-doped

Fig. 2 SEM images of HA and Sr-doped HA nanoparticles
(a) HA; (b) 10%Sr-HA; (c) 50%Sr-HA; (d) 100%Sr-HA

HA nanoparticles are displayed in Fig. 3 and Fig. 4. Fig. 3(a, b) show the morphologies of pure HA nanoparticles. Pure HA displays regular shape and the nanoparticles display rod-like shape. Lengths of most nanoparticles vary from 27.5 to 153.2 nm and the widths of them are between 13 and 27.6 nm. Aspect ratios of crystals are between 2.11 and 7.83. There are no regular morphologies for 10%Sr-HA nanoparticles (Fig. 3(d, e)), which reveals that the crystal structure of HA was distorted because of the doping of Sr ions. As the content of doped Sr increasing to 50%, the irregular crystal size further increased. There was no statistical data about lengths, widths, and aspect ratios of the 10%Sr-HA and 50%Sr-HA nanoparticles due to their irregular shapes. When Sr ions completely replace Ca ions in HA, most of the nanoparticles regain regular shapes as shown in Fig. 3(j, k). The lengths and aspect ratios of the 100%Sr-HA nanoparticles increased significantly compared to those of other three types of nanoparticles, which are consistent with the results obtained by SEM observation. Most of the 100% Sr-HA nanoparticles are between 164.7 and 406.2 nm in length and between 25.5 and 53.9 nm in width. Their aspect ratios varied from 4.33 to 11.01. Morphologies of all types of nanoparticles are consistent with the previous studies[19,24].

HRTEM images corresponding to each type of nanoparticle (Fig. 3(c, f, i, l)) were used to analyze the crystal plane *d*-spacing and crystallinity changes of nanoparticles. Pure HA or Sr-doped HA nanoparticles exhibited good crystallinity, as proved by XRD. In pure HA nanoparticles, most of the observed crystal planes were (002) which had a *d*-spacing of 0.34 nm, and was perpendicular to *c* axis, in consistent with previous study[25]. In the nanoparticles doped with 10at% and 50at% Sr, crystal planes with *d*-spacings of 0.28 and 0.34 nm can be found. When the doping concentration of Sr is 100%, only 0.28 nm crystal plane d-spacing can be observed. SAED patterns (Fig. 4) corresponding to all types of nanoparticles exhibit polycrystalline rings, which is consistent with previous study[18]. These results also demonstrated that all types of nanoparticles had good crystallinity, in consistent with XRD and HRTEM results.

2.5 DFT results

The unit cells of nine Sr-doped HA models after structure optimization are shown in Fig. 5 and Fig. S1. The calculation results obtained by the DFT method are shown in Table 4. To explore the effect of Sr ions doping into HA crystal structures, the lattice parameters of pure HA unit cell were calculated for comparison. Simulation results well confirmed the accuracy of the experimental ones.
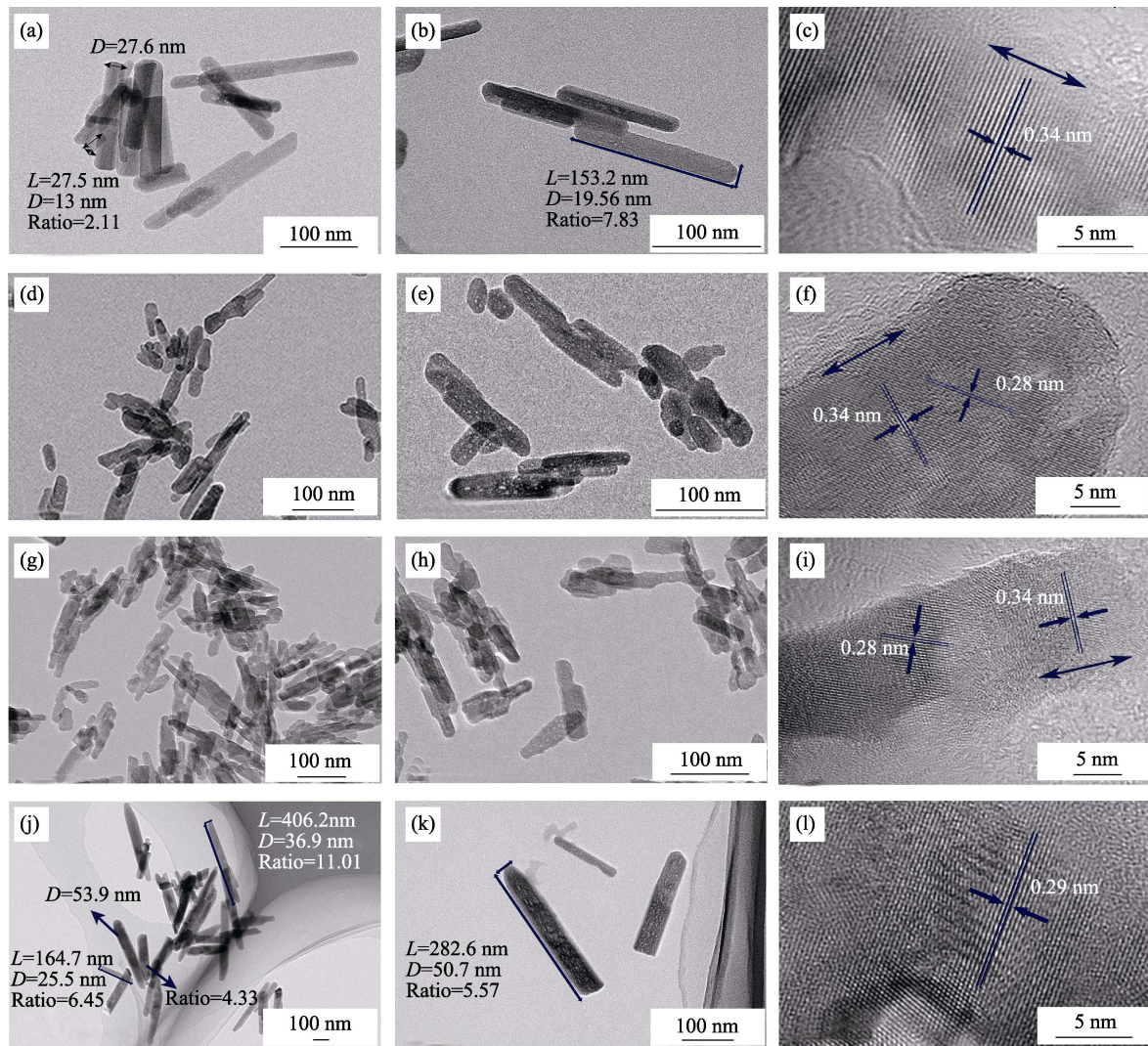
Fig. 3   Morphology of Sr doped HA

(a, b) TEM images of HA; (c) HRTEM image of HA; (d, e) TEM images of 10%Sr-HA; (f) HRTEM image of 10%Sr-HA; (g, h) TEM images of 50%Sr-HA; (i) HRTEM image of 50%Sr-HA; (j, k) TEM images of 100%Sr-HA; (l) HRTEM image of 100%Sr-HA. Scale bars
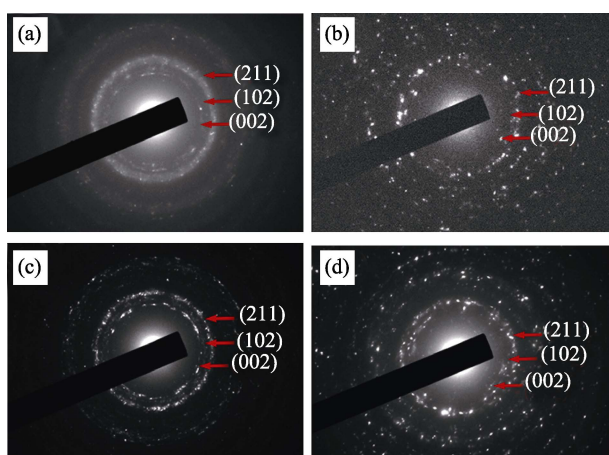

Fig. 4   SAED patterns of samples with different Sr concentrations
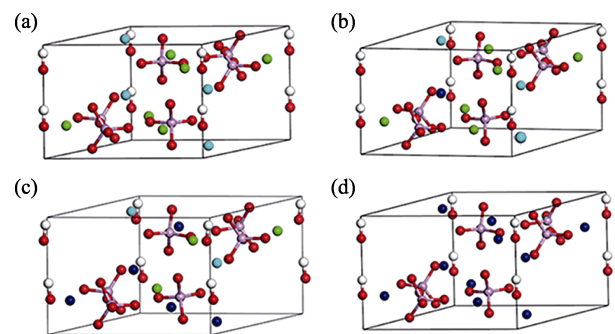(a) HA; (b) 10%Sr-HA; (c) 50%Sr-HA; (d) 100%Sr-HA

Fig. 5   Unit cell of (a) HA, (b) 1Sr-Ca(1)-HA, (c) 2Sr-Ca(1)-3Sr-Ca(2)-HA, (d) 10Sr-HA after structural optimization Calcium (1): light blue; Calcium (2): green; Strontium: dark blue; Phosphorus: pink; Oxygen: red; Hydrogen: white

The lattice parameters (*a-c*) obtained by the simulation method were slightly larger than those provided by the experiment method, as shown in Table 4. Lattice parameters (both *a* and *c*) of all types of Sr-doped HA unit cells distinctly increased with increasing Sr concentrations, no matter which sites [Ca(1) or Ca(2)] were substituted by Sr ions. For 10%Sr-HA models, the lattice

Table 4　Lattice parameters and formation energy calculated by DFT method and lattice parameters (*a* & *c*) obtained from experiments

Method	Model	*a*/nm	*b*/nm	*c*/nm	*V*/nm^3	Formation energy/eV
DFT	HA	0.9642	0.9642	0.6853	5517	
	1Sr-1Ca(1)-HA	0.9695	0.9695	0.6910	5595	−0.307
	1Sr-1Ca(2)-HA	0.9717	0.9727	0.6897	5603	−0.250
	4Sr-4Ca(1)-1Sr-1Ca(2)-HA	0.9724	0.9744	0.7219	5879	−0.404
	3Sr-3Ca(1)-2Sr-2Ca(2)-HA	0.9765	0.9799	0.7159	5897	−0.346
	2Sr-2Ca(1)-3Sr-3Ca(2)-HA	0.9778	0.9841	0.7117	5891	−0.557
	1Sr-1Ca(1)-4Sr-4Ca(2)-HA	0.9788	0.9869	0.7108	5894	−0.369
	5Sr-5Ca(2)-HA	0.9809	0.9861	0.7113	5906	−0.259
	10Sr-HA	0.9922	0.9922	0.7361	6274	−0.321
Experiment	HA	0.9368	–	0.6829	–	–
	10%Sr-HA	0.9463	–	0.6933	–	–
	50%Sr-HA	0.9581	–	0.7106	–	–
	100%Sr-HA	0.9806	–	0.7307	–	–

parameters *a*, *b*, and *c* of 1Sr-Ca(2)-HA and 1Sr-Ca(1)-HA models were larger than those of pure HA model. For 50%Sr-HA and 100%Sr-HA models, the results were roughly the same as that of the 10%Sr-HA model and in line with the previous studies[19,23].

Negative formation energy of all types of Sr-doped HA models suggested that Sr doping enhanced the stability of the apatite crystal structure. For 10at% Sr-HA models, results of formation energy showed that 1Sr-Ca(1)-HA model was more stable than 1Sr-Ca(2)-HA model. At 10at% doping concentration, Sr^{2+} was more likely to replace Ca^{2+} ion at Ca(1) position. Therefore, Ca(1) site was the preferential site for Sr doping at 10%Sr concentration, which was in line with the previous report[27]. For 50%Sr-HA models, 2Sr-Ca(1)-3Sr-Ca(2)-HA model was the most stable model owing to its lowest negative formation energy, which was consistent with the previous study[23].

3　Conclusions

In this work, HA, 10%Sr-HA, 50%Sr-HA, and 100%Sr-HA were prepared by a hydrothermal synthesis method. The conclusions can be drawn as follows:

1) All HA and Sr-doped HA nanoparticles have good crystallinity and show polycrystalline properties. Crystallinity of 10%Sr-HA and 50%Sr-HA are lower than that of pure HA. When Sr concentration reaches 100at%, the crystallinity becomes the highest.

2) Lattice parameters *a* and *c* of HA unit cell increases with increasing concentration of Sr ions. Stabilities of the Sr-HA nanoparticles enhance with the doping of Sr ions due to their negative formation energy. The 2Sr-2Ca(1)-3Sr-3Ca(2)-HA model is more stable than the others because of its minimum formation energy.

Supporting materlals:

Supporting materlals related to this article can be found at https://doi.org/10.15541/jin20180439.

References:

[1] SADAT-SHOJAI M, KHORASANI M T, DINPANAH-KHO-SHDARGI E, *et al*. Synthesis methods for nanosized hydroxyapatite with diverse structure. *Acta Biomaterialia*, 2013, **9(8):** 7591–7621.

[2] LANDI E, TAMPIERI A, MATTIOLI-BELMONTE M, *et al*. Biomimetic Mg-and Mg, CO$_3$-substituted hydroxyapatites: synthesis characterization and *in vitro* behaviour. *Journal of the European Ceramic Society*, 2006, **26(13):** 2593–2601.

[3] WANG H, LEE J K, MOURSI A, *et al*. Ca/P ratio effects on the degradation of hydroxyapatite *in vitro*. *Journal of Biomedical Materials Research Part A*, 2003, **67(2):** 599–608.

[4] SHI Z, HUANG X, CAI Y, *et al*. Size effect of hydroxyapatite nanoparticles on proliferation and apoptosis of osteoblast-like cells. *Acta Biomaterialia*, 2009, **5(1):** 338–345.

[5] THIAN E, KONISHI T, KAWANOBE Y, *et al*. Zinc-substituted hydroxyapatite: a biomaterial with enhanced bioactivity and antibacterial properties. *Journal of Materials Science: Materials in Medicine*, 2013, **24(2):** 437–445.

[6] XIU Z, LÜ M, LIU S, *et al*. Barium hydroxyapatite nanoparticles synthesized by citric acid Sol–Gel combustion method. *Materials Research Bulletin*, 2005, **40(9):** 1617–1622.

[7] GE X, LENG Y, BAO C, *et al*. Antibacterial coatings of fluoridated hydroxyapatite for percutaneous implants. *Journal of Biomedical Materials Research - Part A*, 2010, **95(2):** 588–599.

[8] GE X, LENG Y, REN F, *et al*. Integrity and zeta potential of fluoridated hydroxyapatite nanothick coatings for biomedical applications. *Journal of the Mechanical Behavior of Biomedical Materials*, 2011, **4(7):** 1046–1056.

[9] GE X, REN C, LU X, *et al*. Surfactant-free electrochemical synthesis of fluoridated hydroxyapatite nanorods for biomedical applications. *Ceramics International*, 2019, **45(14):** 17336–17343.

[10] YOUNESS R A, TAHA M A, IBRAHIM M. *In vitro* bioactivity, physical and mechanical properties of carbonated-fluoroapatite during mechanochemical synthesis. *Ceramics International*, 2018,

44(17): 21323–21329.

[11] SEDELNIKOVA M B, KOMAROVA E G, SHARKEEV Y P, *et al*. Modification of titanium surface *via* Ag-, Sr-and Si-containing micro-arc calcium phosphate coating. *Bioactive Materials*, 2019, **4:** 224–235.

[12] BOANINI E, TORRICELLI P, GAZZANO M, *et al*. Combined effect of strontium and zoledronate on hydroxyapatite structure and bone cell response. *Biomaterials*, 2014, **35(21):** 5619–5626.

[13] PENG S, ZHOU G, LUK K D, *et al*. Strontium promotes osteogenic differentiation of mesenchymal stem cells through the Ras/MAPK signaling pathway. *Cellular Physiology and Biochemistry*, 2009, **23(1/2/3):** 165–174.

[14] ZHOU J, LI B, LU S, *et al*. Regulation of osteoblast proliferation and differentiation by interrod spacing of Sr-HA nanorods on microporous titania coatings. *ACS Applied Materials & Interfaces*, 2013, **5(11):** 5358–5365.

[15] LAURENCIN D, WONG A, HANNA J V, *et al*. A high-resolution 43Ca solid-state NMR study of the calcium sites of hydroxyapatite. *Journal of the American Chemical Society*, 2008, **130(8):** 2412–2413.

[16] LI P, JIA Z, WANG Q, *et al*. A resilient and flexible chitosan/silk cryogel incorporated Ag/Sr co-doped nanoscale hydroxyapatite for osteoinductivity and antibacterial properties. *Journal of Materials Chemistry B*, 2018, **6(45):** 7427–7438.

[17] ZEGLINSKI J, NOLAN M, BREDOL M, *et al*. Unravelling the specific site preference in doping of calcium hydroxyapatite with strontium from *ab initio* investigations and Rietveld analyses. *Physical Chemistry Chemical Physics*, 2012, **14(10):** 3435–3443.

[18] GENG Z, CUI Z, LI Z, *et al*. Synthesis, characterization and the formation mechanism of magnesium-and strontium-substituted hydroxyapatite. *Journal of Materials Chemistry B*, 2015, **3(18):** 3738–3746.

[19] BIGI A, BOANINI E, CAPUCCINI C, *et al*. Strontium-substituted hydroxyapatite nanocrystals. *Inorganica Chimica Acta*, 2007, **360(3):** 1009–1016.

[20] TERRA J, DOURADO E R, EON J G, *et al*. The structure of strontium-doped hydroxyapatite: an experimental and theoretical study. *Physical Chemistry Chemical Physics*, 2009, **11(3):** 568–577.

[21] WEBSTER T J, MASSA-SCHLUETER E A, SMITH J L, *et al*. Osteoblast response to hydroxyapatite doped with divalent and trivalent cations. *Biomaterials*, 2004, **25(11):** 2111–2121.

[22] LANDI E, TAMPIERI A, CELOTTI G, *et al*. Densification behaviour and mechanisms of synthetic hydroxyapatites. *Journal of the European Ceramic Society*, 2000, **20(14/15):** 2377–2387.

[23] WANG Q, LI P, TANG P, *et al*. Experimental and simulation studies of strontium/fluoride-codoped hydroxyapatite nanoparticles with osteogenic and antibacterial activities. *Colloids and Surfaces B: Biointerfaces*, 2019, **182:** 110359.

[24] LI Z H, WU J M, HOAN S J, *et al*. Preparation and property of strontium-substituted hydroxyapatite. *Journal of Inorganic Materials*, 2011, **26(1):** 49–54.

[25] LI Z Y, LAM W M, YANG C, *et al*. Chemical composition, crystal size and lattice structural changes after incorporation of strontium into biomimetic apatite. *Biomaterials*, 2007, **28(7):** 1452–1460.

[26] WANG Q, TANG P, GE X, *et al*. Experimental and simulation studies of strontium/zinc-codoped hydroxyapatite porous scaffolds with excellent osteoinductivity and antibacterial activity. *Applied Surface Science*, 2018, **462:** 118–126.

[27] MATSUNAGA K, MURATA H. Strontium substitution in bioactive calcium phosphates: a first-principles study. *The Journal of Physical Chemistry B*, 2009, **113(11):** 3584–3589.

掺锶羟基磷灰石纳米颗粒的合成、表征及模拟研究

周子航[1], 王 群[2], 葛 翔[3], 李朝阳[1]

(1. 天津大学 材料科学与工程学院, 天津 300350; 2. 绵阳师范学院 生命科学与技术学院, 绵阳 621000; 3. 天津大学 机械工程学院, 机构理论与装备设计教育部重点实验室, 天津 300354)

摘 要: 锶(Sr)掺杂羟基磷灰石(HA)在生物材料中得到广泛应用。在此研究中, 使用水热合成的方法制备 HA 和 Sr 掺杂 HA 的纳米颗粒。通过实验和计算机模拟的方法研究 Sr 掺杂对 HA 化学成分、结晶度、晶格参数、形貌和形成能的影响。实验结果表明, Sr 掺杂后的 HA 纳米颗粒晶格参数和晶体尺寸增大。随着 Sr 离子浓度的增加, Sr 掺杂 HA 的纳米颗粒的结晶度没有显著变化。模拟结果验证了实验得到的 Sr 掺杂 HA 纳米颗粒晶格参数的准确性, 且进一步表明 Sr 离子掺杂后纳米颗粒的形成能较低, 结构更稳定。当 Sr 掺杂浓度为10%时, Sr 掺杂的优先位点是 Ca(1); Sr 掺杂浓度为50%时, Sr 混合掺杂到 Ca(1)和 Ca(2)位点为更优先的掺杂模式。

关 键 词: 羟基磷灰石; 锶掺杂; 晶格参数; 密度泛函理论; 形成能

Supporting Materials:

Strontium Doped Hydroxyapatite Nanoparticles: Synthesis, Characterization and Simulation

ZHOU Zihang[1], WANG Qun[2], GE Xiang[3], LI Zhaoyang[1]

(1. School of Materials Science and Engineering, Tianjin University, Tianjin 300350, China; 2. College of Life Science and Biotechnology, MianYang Teachers' College, Mianyang 621006, China; 3. Key Laboratory of Mechanism Theory and Equipment Design of Ministry of Education, School of Mechanical Engineering, Tianjin University, Tianjin 300354, China)
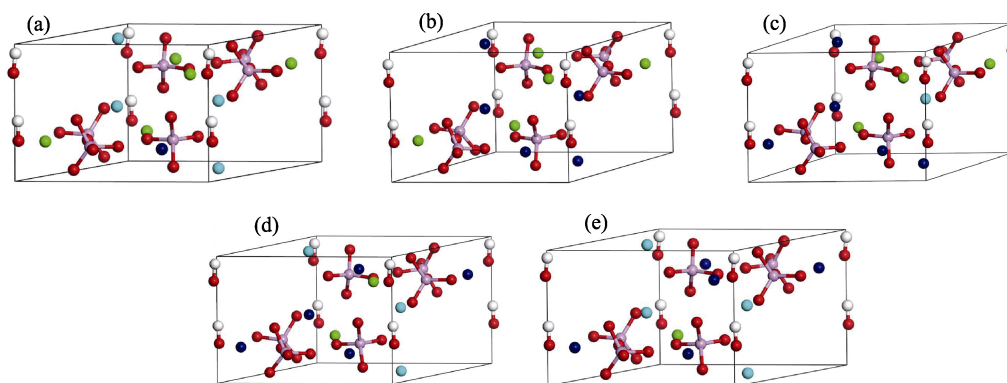

Fig. S1 The unit cell of (a) 1Sr-Ca(2)-HA, (b) 4Sr-Ca(1)-1Sr-Ca(2)-HA, (c) 3Sr-Ca(1)-2Sr-Ca(2)-HA,

(d) 1Sr-Ca(1)-4Sr-Ca(2)-HA, (e) 5Sr-Ca(2)-HA after structural optimization. Color codes: Calcium (1): light blue,

Calcium (2): green, Strontium: dark blue, Phosphorus: pink, Oxygen: red, Hydrogen: white